

Constraints on the nature of dust particles by infrared observations

Cs. Kiss,^{1*} P. Ábrahám,¹ R. J. Laureijs,² A. Moór¹ and S. M. Birkmann³

¹*Konkoly Observatory of the Hungarian Academy of Sciences, PO Box 67, H-1525 Budapest, Hungary*

²*European Space Agency, Astrophysics Division, Keplerlaan 1, 2201AZ Noordwijk, The Netherlands*

³*Max-Planck-Institut für Astronomie, Königstuhl 17, D-69117, Heidelberg, Germany*

Accepted 2006 September 24. Received 2006 September 23; in original form 2006 April 6

ABSTRACT

The far-infrared (FIR) emissivity of dust is an important parameter characterizing the physical properties of the grains. With the availability of stellar data bases and FIR data from *Infrared Space Observatory (ISO)*, it is possible to compare the optical and infrared properties of dust, and derive the FIR emissivity with respect to the optical extinction. In this paper, we present the results of a systematic analysis of the FIR emissivity of interstellar clouds observed with ISOPHOT (the photometer onboard *ISO*) at least at two infrared wavelengths, one close to $\sim 100 \mu\text{m}$ and the other at $200 \mu\text{m}$. We constructed FIR emission maps, determined dust temperatures, created extinction maps using Two-Micron All-Sky Survey data and calculated FIR emissivity for each of these clouds. We present the largest homogeneously reduced data base constructed so far for this purpose. During the data analysis, special care was taken on possible systematic errors. We find that FIR emissivity has a clear dependence on temperature. The emissivity is enhanced by a factor of usually less than 2 in the low dust temperature regime of $12 \text{ K} \leq T_d \leq 14 \text{ K}$. This result suggests larger grain sizes in those regions. However, the emissivity increase of typically below 2 restricts the possible grain growth processes to ice mantle formation and coagulation of silicate grains, and excludes the coagulation of carbonaceous particles on the scales of the regions we investigated. In the temperature range $14 \text{ K} \leq T_d \leq 16 \text{ K}$, a systematic decrease of emissivity is observed with respect to the values of the diffuse interstellar matter. Possible scenarios for this behaviour are discussed in this paper.

Key words: ISM: clouds – dust, extinction – infrared: ISM.

1 INTRODUCTION

The far-infrared (FIR) emissivity of interstellar grains predominantly emitting at wavelengths in excess of $100 \mu\text{m}$ can now be determined in many molecular and moderate density regions thanks to the increasing availability of FIR, submillimetre and massive stellar data sets. Several studies have reported on the detection of an enhancement of the FIR emissivity in the $100\text{--}200 \mu\text{m}$ wavelength range in regions of higher column density compared to the dust emissivity in the diffuse interstellar medium (DISM) associated with H I (Bernard et al. 1999; Cambrésy et al. 2001; Juvela et al. 2002; Stepnik et al. 2003; Lehtinen et al. 2004; Rawlings et al. 2005). The largest sample of different regions is presented in del Burgo et al. (2003) presenting a study of eight translucent clouds.

The observations suggest a trend where the emissivity increases with decreasing temperature. The variation is attributed to a change in grain properties which is expected to take place in denser envi-

ronments. In particular, the increase in emissivity is interpreted as a signature of an enhancement in grain size.

However, the trend shows a large scatter which might be due to the observational limitations which increase the uncertainties. On one hand, star counts statistically probe only a limited extinction range and, on the other hand, the determination of the grain temperatures in the infrared (IR) can have large uncertainties.

In this study, we present a large sample based on *Infrared Space Observatory (ISO)* data of cloud regions with reliable values of the FIR dust emissivity and optical extinction data. We examine in detail the possible observational and data processing errors to ensure the reliability of our results. A general good agreement was found between our results and previous studies of individual regions. Due to the large number of data points, we are able to put stronger constraints on the emissivity changes with temperature.

2 OBSERVATIONS AND DATA REDUCTION

2.1 FIR maps

We searched the *ISO* Archive (Salama 2004) for ISOPHOT observations (Lemke et al. 1996) of interstellar clouds matching the

*E-mail: pkisscs@konkoly.hu

Table 1. Summary table of the basic properties and derived quantities of the fields analysed in this study. The columns of the table are: (1) the name of the field (denoting central galactic coordinates); (2) *ISO* id (TDT number; Laureijs et al. 2003) of the short and long wavelength measurements. (3–4) right ascension and declination of the field centres (J2000); (5) short and long ISOPHOT filter wavelengths used; (6) dust temperature derived from ISOPHOT short versus long wavelength (200 μm) surface brightness scatter plots, the uncertainties presented here reflect the formal errors of the fits only; (7) fitted slope of the 200- μm surface brightness (I_{200}) versus visual extinction (A_V) scatter plot; (8) dust emissivity derived from Columns 6 and 7.

Field	<i>ISO</i> id [$\lambda_{\text{short}}/\lambda_{\text{long}}$]	α_{J2000} (h m s)	δ_{J2000} ($^{\circ}$ ' ")	$\lambda_{\text{short}}/\lambda_{\text{long}}$ (μm)	T_d (K)	I_{200}/A_V ($\text{MJy sr}^{-1} \text{mag}^{-1}$)	τ_{200}/A_V ($\times 10^{-4} \text{mag}^{-1}$)
G004.3+35.8	10101158/10101157	15 53 46	−4 31 19	100/200	14.0 ± 0.2	11.3 ± 0.8	3.9 ± 0.3
G100.0+14.8	40100614/39602313	20 32 45	65 19 49	90/200	16.0 ± 0.1	10.7 ± 0.5	1.9 ± 0.1
G101.8+17.0	80000751/80000652	20 23 19	68 01 55	100/200	14.7 ± 0.4	5.2 ± 1.6	1.4 ± 0.4
G102.0+15.2	40100818/40100717	20 40 06	67 10 43	90/200	15.0 ± 0.0	10.8 ± 0.4	2.6 ± 0.1
G114.0+14.9	75501106/75400905	22 28 06	75 13 22	120/200	13.3 ± 0.3	8.0 ± 1.4	3.6 ± 0.6
G114.0+14.9	75501106/75400905	22 28 06	75 13 22	120/200	12.5 ± 0.3	4.4 ± 0.9	2.8 ± 0.5
G114.3+14.7	75501211/75501210	22 33 03	75 14 38	120/200	12.1 ± 0.6	4.2 ± 0.5	3.3 ± 0.4
G114.6+14.6	76701109/76701108	22 37 45	75 13 13	120/200	12.9 ± 0.1	6.7 ± 0.5	3.5 ± 0.3
G114.6+14.6	76701109/76701108	22 37 45	75 13 13	120/200	12.2 ± 0.1	10.1 ± 0.9	7.4 ± 0.7
G121.6+24.6	56201502/56201701	23 07 27	87 10 30	90/200	15.5 ± 0.1	8.0 ± 0.5	1.7 ± 0.1
G122.0+24.2	56201606/36803005	23 43 45	86 58 18	90/200	14.9 ± 0.1	3.5 ± 0.6	0.9 ± 0.2
G142.0+38.5	15600853/15600851	9 32 57	70 26 12	100/200	15.1 ± 0.2	3.4 ± 0.6	0.8 ± 0.2
G170.2−16.0	85701512/85701411	4 21 20	27 00 42	120/200	13.3 ± 0.3	6.3 ± 1.1	2.8 ± 0.5
G170.2−16.0	85701512/85701411	4 21 20	27 00 42	120/200	12.4 ± 0.3	3.8 ± 1.0	2.5 ± 0.7
G173.9−15.7	68200305/68200403	4 32 41	24 36 18	120/200	12.9 ± 0.2	5.7 ± 0.5	3.0 ± 0.3
G174.3−15.9	68400606/68301104	4 32 58	24 10 51	120/200	13.2 ± 0.1	6.0 ± 0.3	2.8 ± 0.1
G297.3−16.2	26100704/26100703	11 04 19	−77 51 12	100/200	14.4 ± 0.1	5.6 ± 0.3	1.7 ± 0.1
G300.2−16.8	15701656/15701655	11 53 21	−79 21 41	120/200	14.2 ± 0.1	18.4 ± 0.5	5.9 ± 0.2
G301.7−16.6	14102209/14102110	12 25 24	−79 22 47	90/200	15.2 ± 0.2	14.7 ± 1.1	3.4 ± 0.2
G302.6−15.9	27600420/27600419	12 44 55	−78 48 24	100/200	13.8 ± 0.3	9.8 ± 0.9	3.6 ± 0.3
G303.5−14.2	71801760/33300559	13 00 47	−77 06 09	100/200	16.8 ± 0.1	6.5 ± 1.2	0.9 ± 0.2
G303.5−14.2	71801760/33300559	13 00 47	−77 06 09	100/200	13.3 ± 0.1	9.8 ± 0.5	4.5 ± 0.2
G303.8−14.2	71901220/71901119	13 07 04	−77 01 02	100/200	14.7 ± 0.1	5.1 ± 0.9	1.4 ± 0.2
G355.3+14.7	31000632/31000631	16 40 03	−24 11 48	100/200	15.6 ± 0.5	5.7 ± 1.1	1.1 ± 0.2
G359.1+36.7	43100630/43100629	15 40 09	−7 12 29	100/200	16.1 ± 0.1	13.0 ± 0.5	2.3 ± 0.1
G359.9−17.9	33401134/33401133	19 02 18	−36 59 31	100/200	15.4 ± 0.4	8.6 ± 1.6	1.8 ± 0.3
G089.0 − 41.2*	21600513/21600514	23 08 35	14 45 45	90/200	16.3 ± 0.2	12.8 ± 3.9	2.1 ± 0.6
G111.2+19.6*	11100606/11101606	21 02 16	76 51 50	150/200	15.2 ± 0.2	13.9 ± 1.5	3.1 ± 0.3
G187.3 − 16.7*	82901031/82901031	5 02 24	13 41 15	120/200	14.6 ± 0.1	12.2 ± 0.8	3.3 ± 0.2
G297.3 − 15.7*	26101501/26101401	11 07 55	−77 28 15	150/200	14.7 ± 0.1	7.0 ± 0.4	1.9 ± 0.1
G301.2 − 16.5*	60601027/60601027	12 16 22	−79 17 09	120/200	13.2 ± 0.1	8.9 ± 1.0	4.1 ± 0.4
G301.7 − 16.6*	60600925/60600925	12 25 24	−79 22 47	120/200	12.8 ± 0.1	19.4 ± 3.1	10.5 ± 1.7

following criteria. (i) The field has been covered at least at two FIR wavelengths: one at 200 μm (*long*) and the other at either 90, 100 or 120 μm (*short*) in order to provide a sufficient wavelength interval for a reliable colour temperature calculation; (ii) the cloud has to be galactic and must have sufficient dynamic range in brightness for correlation analyses; (iii) the map is larger than 5 arcmin at least in one dimension and (iv) there is no high-mass star formation going on in the vicinity of the cloud which could significantly change the local interstellar radiation field. In total, we selected 22 maps which is the largest sample evaluated so far for studying FIR dust emissivity. All selected maps were obtained with the P22 astronomical observing template mode (Laureijs et al. 2003). Measurement wavelengths, *ISO* id numbers and central positions are listed in Table 1.

The ISOPHOT observations were performed with the C100 (43.5×43.5 arcsec² sized pixels) and C200 (89.5×89.5 arcsec² sized pixels) cameras. The ISOPHOT data were processed with the PHOT Interactive Analysis software version 10.0 (PIA; Gabriel et al. 1997), using standard batch processing and a first quartile flat-fielding. We followed in detail the processing scheme described in del Burgo et al. (2003). The data were colour corrected taking into account the dust temperature derived from the brightness ratio at the two wavelengths (see Section 3.1).

The officially quoted absolute photometric uncertainty of the surface brightness in the *ISO* Legacy Archive is ≤ 20 –25 per cent (Klaas et al. 2003). In the present study, we estimated independently this uncertainty in two ways. We compared the ISOPHOT and *COBE/DIRBE* (Diffuse Infrared Background Experiment) background surface brightness values, interpolated to the ISOPHOT wavelengths (i) for a large sample of minimap observations and (ii) for our target fields. This analysis is presented in Appendix A. The results of this investigation show that the typical relative deviations of the individual ISOPHOT measurements with respect to the *COBE/DIRBE* values are ~ 15 per cent, and that there is no notable systematic discrepancy between the two photometric systems. Throughout this paper, we present our results in the ISOPHOT/PIA 10.0 surface brightness photometric system. The effect of a potential imperfect surface brightness calibration is discussed in detail in Section 4.5, based on results presented in Appendix A.

2.2 Extinction data

The traditional method to derive extinction in interstellar clouds is based on variations in stellar density in the sky due to the obscuration of dust (Wolf 1923). Star counts obtained by placing a regular grid on the target field are converted to *B*- or *V*-band extinction

using statistical methods; the zero extinction level is obtained by comparison with a nearby extinction-free reference field.

Cambr esy et al. (1997) replaced the classical regular grid with an adaptive one; in this method, the gridsize is adjusted to include a fixed number of stars, therefore it can still provide extinction estimates for high-density regions. However, in these cases the derived A_V values are averages over the enlarged area of the adaptive cell.

Due to the requirement of sufficient count of stars for reliable statistics, the minimum resolution is limited to arcmin scales, and low dust column densities. The maximum extinction in the visual is at best 5 mag and cannot be improved significantly by deep dedicated observations. In that respect, online catalogues with optical stellar data are well suited for the method.

In recent years, the application of near-infrared (NIR) reddening of individual stars has become widely used due to the general availability of J -, H - and K -band measurements. Extinction mapping methods using NIR reddening often combine the individual reddening values in some statistical manner in order to minimize the effect of individual line of sights. The Near-Infrared Colour Excess (NICE) and Near-Infrared Colour Excess Revisited (NICER) colour excess methods (Lada et al. 1994; Lombardi & Alves 2001) proved to produce good quality maps in many applications. Although NIR star counts are more reliable for high extinction values, in the low to intermediate extinction range ($A_V \leq 15$ mag) the NIR colour excess methods are superior over NIR star counts since they are less affected by the presence of foreground stars (Cambr esy et al. 2002).

The Two-Micron All-Sky Survey (2MASS) Point Source Catalogue (Cutri et al. 2003) is a powerful source of NIR data and can be used to obtain NIR colour excess/extinction as was done by many authors in recent years.

A detailed comparison of visual extinctions obtained by optical star count and NIR colour excess is presented in Kiss et al. (2006).¹ In this paper, extinction maps are derived using star counts of United States Naval Observatory (USNO) data (Monet, Bird & Canzian 1998; Monet, Levine & Canzian 2003) and using NIR (J , H and K_S band) reddening of 2MASS data. Their fig. 2 shows a good correlation of the two data sets and the slope of the scatter plot is very near to unity for low extinctions. A flattening of the USNO extinction occurs at 3–3.5 mag, due to the already insufficient count statistics at these extinction levels.

The NIR colour excess methods are less affected by uncertainties due to foreground stars and give reliable extinction values in denser regions up to ~ 15 mag. Therefore, we decided to apply the NICER method on the 2MASS Point Source Catalogue to obtain extinction maps in this paper. Following the findings by Cambr esy et al. (2002), we set $A_V^{\text{lim}} = 8$ mag for the limiting magnitude of 2MASS data, assuming a 10 per cent of foreground stars in the target field. Above this limit, we did not consider the extinction data to be reliable. These data points were excluded from the further analysis. Due to the low number of data points above this limit and outlier resistant routines we used in the scatter plot analysis, difference between the effect of a cut in A_V or of a cut perpendicular to the slope at $A_V^{\text{lim}} = 8$ mag is negligible.

3 RESULTS

3.1 Dust temperature

We derived colour temperatures T_d from the slope in the I_{λ_1} versus I_{λ_2} scatter plot of a specific sky region, where I_{λ_1} and I_{λ_2} are the

¹ Note that the first author of the cited paper is *not* the first author of the present paper.

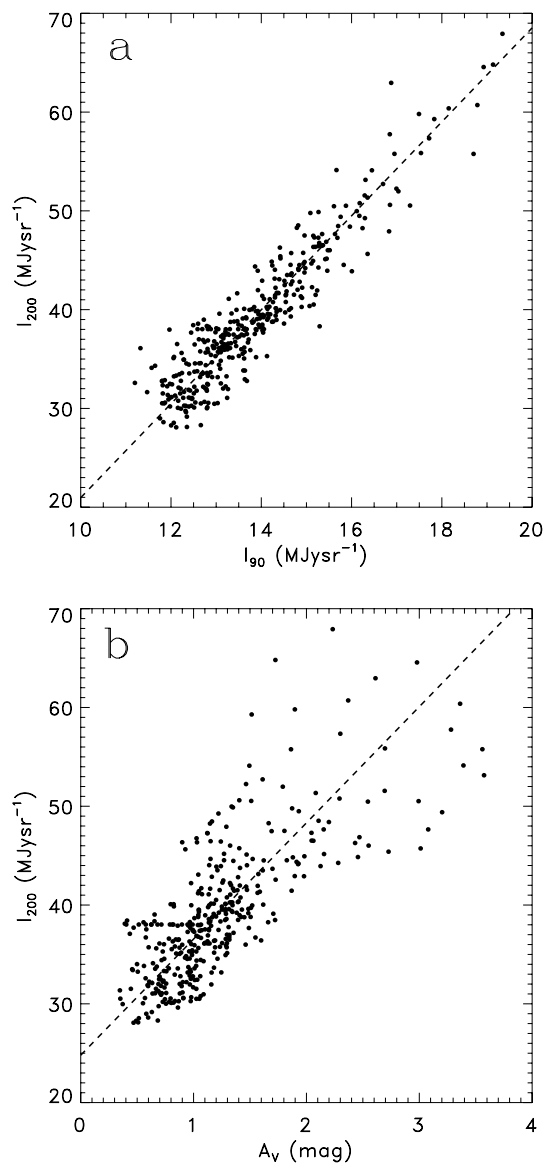


Figure 1. Example (a) of a short versus long wavelength surface brightness scatter plot and (b) a visual extinction versus 200- μm surface brightness scatter plot, both in the G100.0+14.8 field. On both panels, the dashed lines show the fitted lines.

surface brightness values at the wavelengths λ_1 and λ_2 , respectively. An example is shown in Fig. 1(a). Maps taken with the C100 camera (90 and 100 μm) were smoothed to the resolution of the 200- μm observation. The method of using scatter plots to determine T_d is described in del Burgo et al. (2003). It has the main advantage that the slope is insensitive to surface brightness offsets due to e.g. zodiacal light, extragalactic background, calibrational zero-point, etc. The conversion of the $\Delta I_{\lambda_1} / \Delta I_{200}$ slopes to T_d was done via high-resolution $\Delta I_{\lambda_1} / \Delta I_{200} - T_d$ tables, assuming a $\nu^\beta B_\nu(T)$ spectral energy distribution. The tables also accounted for the correct colour correction. We adopted $\beta = 2$.

In Section 4.3, we check the effect of a different emissivity law. In the following, we adopt T_d as an approximation of the physical temperature of the dust grains. del Burgo et al. (2003) found that the scatter plots of some fields can consist of more than one linear section, indicating multiple dust temperatures within the field.

Inspection of the maps of these fields indicated that the different temperature components came from interlocked regions which could be separated by A_V isocontours. The resulting I_{λ_1} versus I_{200} scatter plots of the subfields were sufficiently linear.

The uncertainty in the temperature T_d can be attributed to, first, the error in the slope δ ($\Delta I_{\lambda_1}/\Delta I_{200}$), and, secondly, the calibration uncertainty in the surface brightness values. The first component was computed from the formal uncertainty of the linear fits. The second component was evaluated by using surface brightness uncertainty values given in Section 2.1. The resulting temperature and uncertainty values are typically of the order of 0.7 K depending on the colour temperature (Table 1).

3.2 Emissivity parameters

In Table 1, we list the derived values of I_{200}/A_V obtained from the slopes of the I_{200} versus A_V relationships in those regions, where T_d is constant as delineated by a constant I_{λ_1} versus I_{200} . The 200- μm surface brightness was smoothed to the resolution of A_V . The ratio I_{200}/A_V consists of two independent observables and therefore also serves as a good diagnostics of the main uncertainties. An example A_V versus I_{200} scatter plot is presented in Fig. 1(b).

Using the measured value of T_d from the ratio I_{λ_1}/I_{200} , we derive the ratio between the IR and optical opacity τ_{200}/A_V from $\tau_{200}/A_V = (I_{200}/A_V) B_{200}(T_d)^{-1}$, where $B_{200}(T_d)$ is the Planck function at 200 μm at the dust temperature T_d .

Altogether, we derived 26 sets of T_d , I_{200}/A_V and τ_{200}/A_V values in the 22 maps, due to multiple temperature components in four fields. In addition, six fields of the del Burgo et al. (2003) sample have been reprocessed following our scheme (see Table 1).

The errors of τ_{200}/A_V come from two sources: from the error in the determination of τ_{200}/A_V in the I_{200} versus A_V scatter plot and from the temperature uncertainty in $B_v(T)$. Assuming that these two sources are independent, the final τ_{200}/A_V errors can be expressed via the partial derivatives by τ_{200}/A_V and $B_v(T)$, following standard error propagation. Since we use the slope of the I_{200} versus A_V relation only, systematic offsets in I_{200} and A_V – as in the temperature computation – do not play a role.

To determine the propagation of the error in T_d in the Planck function, we use the two values $T - \delta T$ and $T + \delta T$ to estimate the upper and the lower error bars in τ_{200}/A_V . In most cases, the upper and lower error bars are nearly similar; therefore we give one average value for the uncertainty in Table 1. In the subsequent figures, we present these upper and lower error bars individually. The relative errors caused by the temperature uncertainties are typically much larger than the relative errors from the determination of τ_{200}/A_V in the scatter plots.

3.3 Emissivity versus temperature relationships

In Fig. 2, we present the resulting ratios of I_{200}/A_V and τ_{200}/A_V as a function of T_d for our sample of targets, including the reprocessed del Burgo et al. (2003) sample. In addition, we included in Fig. 2(b) the values obtained by different authors (for references, see figure caption). The I_{200}/A_V ratios of the different studies were made consistent by converting to $\lambda = 200 \mu\text{m}$ assuming a modified blackbody with a $\beta = 2$ emissivity law. The τ_{200}/A_V values from other authors, which were originally obtained at longer wavelengths, were transformed to 200 μm as well. A comparison of our results with these previous works is presented in Section 5.1.

In Fig. 2, the dashed line marks the value of the dust emissivity representative of the DISM. Note that the DISM itself has a unique

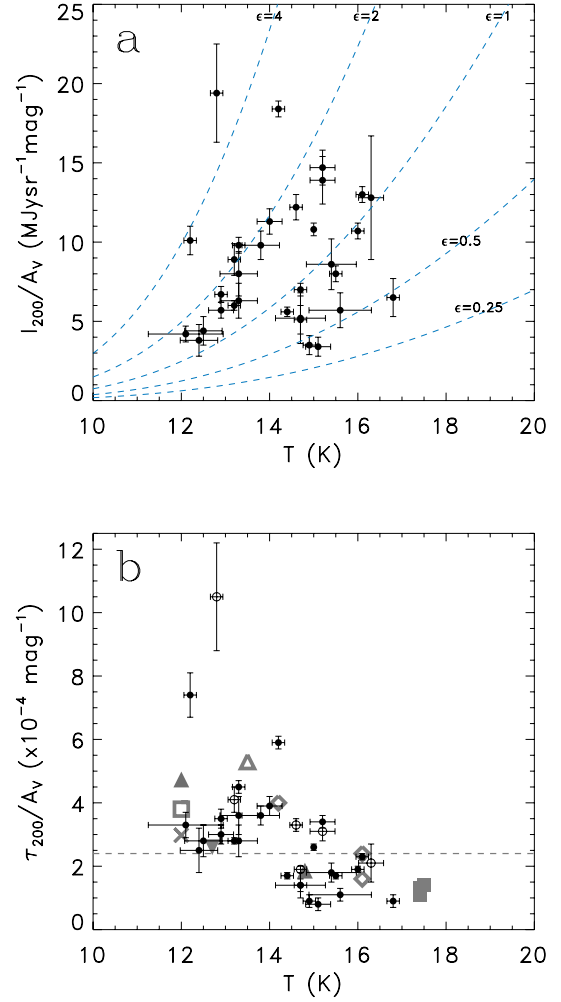


Figure 2. (a) Relationship between I_{200}/A_V and the dust temperature. Dashed lines represent iso-emissivity ($\epsilon = [\tau_{200}/A_V]/[\tau_{200}/A_V]_{\text{DISM}} = \text{constant}$) curves. The corresponding emissivity values are indicated. (b) Relationship between the 200- μm emissivity (τ_{200}/A_V) and the dust colour temperature. Black dots with error bars mark the fields investigated in this study. Open circles with error bars mark the reprocessed del Burgo et al. (2003) target fields. We also present recent results published in other papers, marked by grey symbols – filled triangles: Stepnik et al. (2003); – filled, upside down triangle: Pagani et al. (2003); – filled squares: Rawlings et al. (2005); – cross: Bianchi et al. (2003); – open triangle: Lehtinen et al. (1998); – open diamonds: Lehtinen et al. (2004); – open square: Juvela et al. (2002).

temperature of ~ 17.5 K. The observed values of τ_{200}/A_V exhibit significant deviations from this reference value as a function of temperature. Fields above a dust temperature of 14 K show lower emissivity value than that of the DISM with no obvious trend in their distribution. In the colder fields, emissivity values are above that of the DISM with a weak indication of a decreasing trend towards lower temperatures.

A few points are above the typical emissivity values found for the majority of the fields at low temperature. The higher uncertainties in these fields – as derived from the uncertainties of the temperature and τ_{200}/A_V ratio determination – cannot explain the high τ_{200}/A_V values observed. Further potential sources of systematic errors that could lead to incorrect emissivity values are discussed in detail in Section 4.

4 UNCERTAINTIES IN THE COMPUTATION OF EMISSIVITY PARAMETERS

The reliability of the final emissivity values derived for our target fields may be affected by several sources of errors. This is especially true, if a certain source of error does not contribute only to the random scatter of the derived values, but causes a certain pattern, which may be mistaken for a physical change in dust properties. In this section, we investigate several potential error sources, and try to estimate their impact on the final emissivity determination.

4.1 Derivation of the correct extinction value

The extinction value A_V depends on the wavelength regime and the method used to derive it. In Section 2.2, we compared the results from the USNO star count and the NIR NICER method and concluded that the latter one is more suitable for our study.

The presence of foreground stars may also have an effect on the derived visual extinction values. While in a low extinction part of the cloud most stars in the beam are background objects, towards the densest peaks the stellar sample in the beam may be dominated by foreground stars. As a result, the visual extinction in the densest parts can be underestimated, and the emissivity value overestimated.

Since the foreground objects show low $E(B - V)$ values, we minimized the bias they cause by using an outlier resistant method to calculate the average reddening value in each cell in the NICER method. However, all of our target clouds are nearby (closer than a few hundred parsecs) and are located at high Galactic latitudes ($b \geq 15^\circ$), therefore the contribution of foreground stars is negligible.

The extinction value may also depend on the size of the grid and whether it is of fixed or adaptive type grid. Calculation of extinction/reddening using an adaptive gridsize may significantly underestimate the extinction, especially in a cloud centre, due to an inhomogeneous distribution of stars in the cells. We therefore preferred to use a fixed gridsize in our analysis.

4.2 Dependency of R_V

The ratio of total over selective extinction R_V is found to be significantly higher in dense interstellar clouds than R_V in the DISM (Cardelli et al. 1989; Whittet et al. 2001). This change is a strong indicator that the optical properties of dust grains differ in dense regions. When we derived A_V from A_J by following the method of Lombardi & Alves (2001), we adopted $R_V = 3.1$, which is a value typical for the DISM and may not be representative for the regions we investigate.

Applying the empirical relationship between R_V and A_J/A_V as determined by Cardelli et al. (1989), we find $A_J/A_V = 0.282$ and 0.334 , for $R_V = 3.1$ and 5.5 , respectively, implying that A_V will decrease by 19 per cent when increasing R_V from values representative of the DISM to dense lines of sight. The corresponding τ_{200}/A_V and τ_{200}/A_V values will increase accordingly by 19 per cent. We infer that the uncertainty in the assumption of $R_V = 3.1$ in the determination of A_V has a relatively minor implication on the values of the observables presented in this paper. The assumption may introduce an underestimation of at most 20 per cent in both τ_{200}/A_V and I_{200}/A_V .

4.3 Application of a different emissivity law

Assuming that the exponent of the emissivity law β is close to 2 in the ISM (Gezari, Joyce & Simon 1973; Draine & Lee 1984; Boulanger

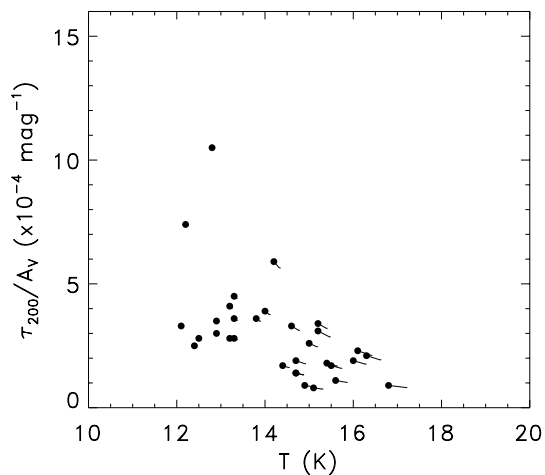


Figure 3. Displacement of τ_{200}/A_V versus T_d data points due to the effect of a temperature-dependent β (Dupac et al. 2003). The original emissivity values with $\beta = 2$ are marked by filled circles. The stripes originating from these points indicate the change due to a different β .

et al. 1996), we adopted $\beta = 2$ to derive T_d from the slope of the short (90, 100 or 120 μm) versus long (200 μm) wavelength scatter plots (Section 3.1).

Based on balloon-borne submillimetre observations of a large number of ISM regions, Dupac et al. (2003) found that β is not constant but depends on the dust temperature as $\beta(T) = [0.4 + 0.008 (T/1 \text{ K})]^{-1}$.

We used this relationship to investigate the effect of possible changes in β on our results. We calculated the new colour temperature from the I_{short} versus I_{200} scatter diagrams using $\beta(T)$. From this temperature, we obtained the modified values for τ_{200}/A_V .

In Fig. 3, we show the effect of $\beta(T)$ on the temperature versus emissivity relationship. The β dependency tends to increase the temperature, but the change is small, only for temperatures higher than 15.5 K the variations are notable, more than 0.3 K but less than 0.5 K. Although the new temperature dependence of β causes a systematic change of the distribution of the measurements in Fig. 3, the effect is small with respect to the measurement uncertainties.

4.4 Presence of warm dust

IRAS-related studies of the dense and DISM have shown that extended emission at 60 μm can be associated with dust in low density regions. In these regions, the 100- μm emission is closely correlated with the 60- μm emission, suggesting that they trace the same dust component in the ISM. At higher densities, the 60- μm emission becomes weak indicating the absence of grains giving rise to the 60- μm emission. The remaining 100- μm emission is a signature of a ‘cold’ dust component at $T < 15$ K. This observation is supported by the close correlation of the cold dust component with ^{13}CO emission. The surface brightness measured at a wavelength of $\lambda \approx 100 \mu\text{m}$ may contain emission from both the cold and the ‘warm’ (or low density) dust component. The warm component will affect the determination of the I_V/I_{200} colour temperature, such that the temperatures will be overestimated due to the short wavelength emission component.

To determine the fraction of the cold component in our short wavelength ($\sim 100 \mu\text{m}$) maps, we analysed 60- and 100- μm maps of our regions obtained with IRAS/IRAS Sky-Survey Atlas (ISSA) because in most fields there are no ISOPHOT observations at

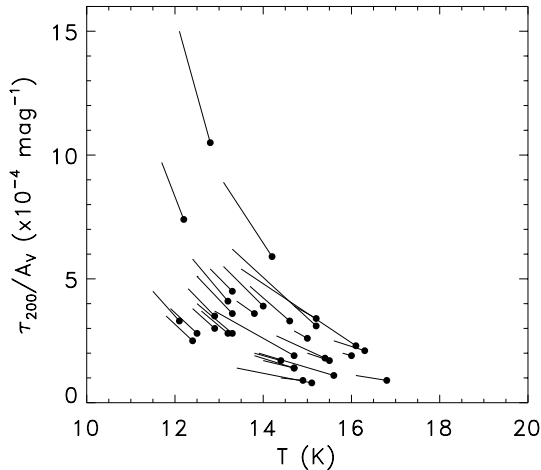


Figure 4. Displacement of the $T_d - \tau_{200}/A_V$ data points with the correction for the warm dust component of the short wavelength surface brightness values. The original data points are marked by filled circles, and the stripes originating from them indicate the change due to the correction for the presence of warm dust.

60 μm . The amount of emission from the cold component at 100 μm towards a specific sky position can be calculated from the two *IRAS* bands:

$$I_{\text{cold}} = I_{100} - \theta I_{60}, \quad (1)$$

where θ is the slope of a linear relationship fitted to the 60- versus 100- μm surface brightness correlation diagram in the outer parts of the cloud. The relative contribution of the cold dust component at 100 μm is estimated from the correlation between I_{cold} and the original I_{100} surface brightness. The scatter diagram was fitted by a linear function, resulting in a slope X_{100} , which gives the ratio of the cold dust emission to total surface brightness at 100 μm . We find typical values of $0.7 \leq X_{100} \leq 0.8$. We used X_{100} to determine the cold dust emission contribution in the ISOPHOT short wavelength bands. Since the ISOPHOT measurements were not always taken at 100 μm , we converted X_{100} to X_λ assuming that the spectral energy distribution of the total surface brightness can be approximated by two modified blackbodies ($\beta = 2$) with two different temperatures, T_{warm} and T_{cold} . We fixed T_{warm} to 17.5 K (Lagache et al. 1998) and set T_{cold} to the temperature obtained from the original surface brightness scatter plots. Our analysis shows that X_λ/X_{100} is close to 1 and the ratio is not very sensitive to T_{cold} . These X_λ values were applied to the short wavelength surface brightness values at 90, 100 or 120 μm , to compute the corrected τ_{200}/A_V values. The results are presented in Fig. 4. The figure shows that the presence of warm dust tends to overestimate the temperature by 0.5–1 K which is significant. As a result, due to the lower temperature of the cold dust and since I_{200}/A_V is hardly affected, correction for warm dust emission increases τ_{200}/A_V by at most 30 per cent.

4.5 Effect of surface brightness calibration errors

Errors in the ISOPHOT surface brightness calibration may affect the derived dust temperatures and the relationships presented in Fig. 2. Here, we first discuss the general effect of surface brightness calibration errors applying a simple model in Section 4.5.1.

Actual calibrational errors in this photometric system can only be unravelled by a comparison with a standard system. Due to its mea-

surement design, the DIRBE instrument onboard the *COBE* satellite was able to perform accurate absolute photometric observations (Hauser, Arendt & Kelsall 1998a) and serves now as the standard system for IR sky brightness observations. A detailed comparison of the surface brightness photometric systems of ISOPHOT and that of *COBE*/DIRBE is presented in Appendix A. In Section 4.5.2, we apply the ISOPHOT–DIRBE surface brightness transformation equations found in Appendix A, and discuss their effect on our results.

4.5.1 General effect of calibration errors

In order to test the effect of the surface brightness calibration errors on the derived emissivities, in a simple approach we assumed a linear relationship between the true sky brightness and the surface brightness measured by a specific instrument/filter, i.e. the transformation equation between the two can be written as

$$I_\lambda^{\text{meas}} = G_\lambda I_\lambda^{\text{sky}} + C_\lambda, \quad (2)$$

where I_λ^{meas} is the measured sky brightness, I_λ^{sky} is the real sky brightness and G (gain) and C (offset) are the coefficients describing the transformation.

Our analysis method, which is based on slope fitting in scatter plots (see Section 2), is not sensitive to errors due to constant offsets in the surface brightness. Multiplicative errors, however, change both the colour temperature and the emissivity parameters. Such errors may come from the presence of a gain uncertainty due to incorrect surface brightness calibration. We investigated the impact of this effect on our emissivity values, using a simple model. We assumed that $I_{\text{short}}^{\text{meas}} = G_{\text{short}} I_{\text{short}}^{\text{sky}}$ and $I_{200}^{\text{meas}} = G_{200} I_{200}^{\text{sky}}$, where $I_{\text{short}}^{\text{sky}}$ and I_{200}^{sky} are the true surface brightness values of the sky at our short wavelength (either 90, 100 or 120 μm) and at 200 μm , respectively, while $I_{\text{short}}^{\text{meas}}$ and I_{200}^{meas} are the values affected by calibration errors. G_{short} and G_{200} are the detector gains for the short wavelength and for the 200- μm filters, respectively. For both G_{short} and G_{200} , we assumed two extrema, 0.91 and 1.09, corresponding to an uncertainty value of 9 per cent, as found for the ISOPHOT filters in Appendix A.

The effect of the four gain combinations for the derived emissivity values and dust temperatures is presented in Fig. 5(a). The shorter, fully vertical lines originated from the black dots correspond to the cases, where both G_{short} and G_{200} have the same value (either the same 0.91 or 1.09). In these cases, the changes in the τ_{200}/A_V values are 9 per cent.

The longer, tilted lines correspond to the cases, when G_{short} and G_{200} have opposite values. Then the amount of change in τ_{200}/A_V and T_d depends notably on the original temperature, but in general is 25–30 per cent. This is a major effect, but the τ_{200}/A_V values remain in the domain, that their relative deviations from the emissivity of the diffuse interstellar matter is still significant.

The difference between the original and recalculated dust temperatures is of the order of ~ 0.7 K. As discussed in Section 3.1, these calibration errors are the main sources of uncertainty in the temperature determination.

The scenario presented here is indeed a ‘worst-case’, i.e. the relative effect of the calibration errors at the two wavelengths is the strongest. The likely effect is smaller and would result in a final τ_{200}/A_V uncertainty of 10–20 per cent, depending on the original colour temperature. Here, we also did not take into account the systematic calibrational differences between the two photometric systems, which could significantly reduce the final τ_{200}/A_V uncertainties (see Section 4.5.2).

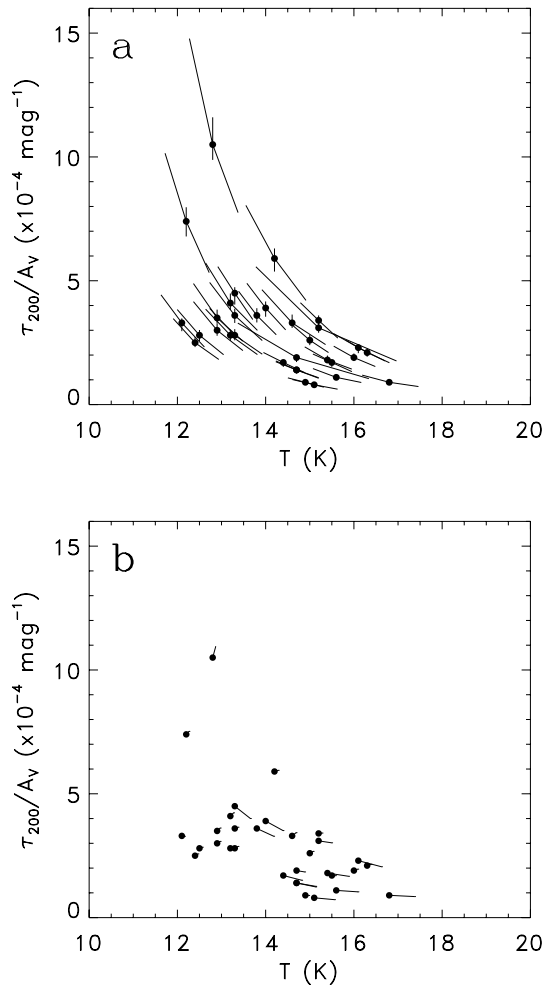


Figure 5. Effect of calibration errors in the surface brightness calibration. (a) Statistical errors in the short and long wavelength surface brightness (see the text for details). The four lines originating from each black dot (the original τ_{200}/A_V data points) span a banana shaped area in the figure, corresponding to 9 per cent calibration errors in both the short and long wavelength ISOPHOT surface brightness values, as found in Appendix A. (b) Displacement of the τ_{200}/A_V values (stripes) relative to the original ones (black dots, as listed in Table 1), when the correlation coefficient between the ISOPHOT and DIRBE surface brightness calibration (see Appendix A) is applied.

4.5.2 Effect of transformation between the ISOPHOT and COBE/DIRBE surface brightness photometric systems

We tested the effect of the correction of ISOPHOT surface brightness values by the ISOPHOT–DIRBE transformation coefficients found in Appendix A (see Table A1). Both the dust temperatures and the τ_{200}/A_V ratios have been recalculated by the corrected surface brightness values in order to obtain the corrected τ_{200}/A_V emissivities. The results are shown in Fig. 5(b). The effect of this correction is small for the τ_{200}/A_V values obtained from measurements with the 90- and 120- μm ISOPHOT filters. The 100 μm related data points are more displaced, due to the relatively large difference in the scaling factors. However, the overall shape of the distribution did not change significantly, and the effect is much smaller than that of the general calibration errors presented in Section 4.5.1.

4.6 The impact of various error sources on the emissivity–dust temperature relationship

The distribution of data points in Fig. 2(b) indicates a clear trend in the τ_{200}/A_V versus T relationship: τ_{200}/A_V is enhanced for $T < 14$ K and decreases towards higher temperatures in the range $14 \leq T \leq 16$ K. In the preceding subsections, we investigated possible mechanisms which could explain this observation, our findings are summarized below.

(i) 2MASS data provide reliable extinction maps for our regions. Contamination by foreground stars – which is most critical towards the densest regions – cannot be excluded, but probably has a minor effect.

(ii) The dense clouds in our sample, presumably also the cold ones, may have a ratio of total over selective extinction R_V higher than the standard value of 3.1. As a consequence, A_V may decrease at most by ~ 19 per cent, and the corresponding τ_{200}/A_V and τ_{200}/A_V values increase accordingly by the same fraction. However, high R_V should be restricted to small areas in our target fields. These regions are probably excluded anyhow due to their too low star count or too high extinction values ($A_V \geq 8$ mag). Therefore, the likely effect of R_V on the final emissivity values is below ~ 10 per cent.

(iii) Assuming a temperature-dependent emissivity law $\beta(T)$ instead of a fixed $\beta = 2$ has a minor effect on the τ_{200}/A_V distribution (Fig. 3). The differences with $\beta = 2$ are more prominent at higher temperatures, but the main trend for clouds colder than the dust in the DISM is not changed.

(iv) The possible presence of warm dust causes an overestimate of the dust temperature and, consequently, an underestimate of τ_{200}/A_V by 10–30 per cent. This variation is within the typical measurement uncertainties of the data points and does not alter the trend as observed in Fig. 2.

(v) Calibration errors can significantly modify the τ_{200}/A_V and dust temperature values. The application of ISOPHOT surface brightness values corrected for the systematic differences of the ISOPHOT and COBE/DIRBE surface brightness photometric systems does not change the observed distribution of τ_{200}/A_V values significantly. Applying a ± 9 per cent general calibration uncertainty would cause a much severe effect, but the corrected results remain in the ~ 25 per cent range to the original values. Transformation of the ISOPHOT surface brightness values to the DIRBE photometric system has only a minor effect on the T_d versus τ_{200}/A_V relationship.

From the uncertainties due to different error sources, we estimated a general ~ 30 per cent uncertainty for our τ_{200}/A_V values. To match the observations by assuming a constant emissivity, (that of the DISM) a 50–80 per cent uncertainty is required, which is unrealistic, according to our investigations. The observed temperature versus τ_{200}/A_V relationship, as presented in Fig. 2(b), most probably indicates physical changes and is *not* due to artefacts in the data or to incorrect initial assumptions in the calculations.

5 DISCUSSION

5.1 Observed variations in τ_{200}/A_V

We found notable differences between the original del Burgo et al. (2003) τ_{200}/A_V values and the emissivities of the same fields re-processed in this paper. The main differences between our and the del Burgo et al. (2003) processing are that in this study we applied extinction values derived from 2MASS data and used different short

wavelength data for the temperature calculation, namely 90, 100 or 120 μm instead of 150 μm . (These new results are also included in Table 1 and in Fig. 2.) The dust temperatures we found are consistent with those in del Burgo et al. (2003). However, the resulting τ_{200}/A_V ratios are different, and this discrepancy leads to notably lower τ_{200}/A_V values (see Table 1). This also indicates that it is mainly the application of 2MASS data that is responsible for the differences seen in the emissivities.

Our values obtained for the TMC 2 (G173.9–15.7 and G174.3–15.9) and for LDN 1780 (G359.1+36.7) are very similar to the average values presented for these clouds by del Burgo & Laureijs (2005) and Ridderstad et al. (2006), respectively. In these papers, I_{200}/A_V and τ_{200}/A_V values were derived by taking the brightness ratios from the maps instead of correlation plots. Despite the general agreement with our data, the detailed analysis of LDN 1780 shows that τ_{200}/A_V can range from 10^4 mag^{-1} to $4 \times 10^4 \text{ mag}^{-1}$ within the same cloud (Ridderstad et al. 2006). An even higher increase of τ_{200}/A_V is observed in the Taurus 2 molecular cloud (del Burgo & Laureijs 2005).

An important outcome of our analysis of a large sample of cloud regions is that we find a clear trend of τ_{200}/A_V versus T_d , but that the variation in τ_{200}/A_V is less pronounced than initially reported by other studies. Only three fields exhibit τ_{200}/A_V , which is more than threefold, the value for the DISM ($\tau_{200}/A_V \text{ DISM}$). All other regions with $T_d < 14 \text{ K}$ (12 regions) have $\tau_{200}/A_V > \tau_{200}/A_V \text{ DISM}$. In the majority of the regions with $T_d > 14 \text{ K}$, the emissivities are below $\tau_{200}/A_V \text{ DISM}$ (10 out of 12 regions). One extreme case is G142.0+38.5, where $3\tau_{200}/A_V \approx \tau_{200}/A_V \text{ DISM}$.

The values of τ_{200}/A_V in our sample refer to the average properties (T_d , and τ_{200}/A_V) over a relatively extended region of $\sim 100 \text{ arcmin}^2$. The enhancement, observed by us, of $\epsilon < 2$ in most cases suggests that higher ϵ values usually occur only in smaller regions inside the clouds, possibly in the densest cores.

We have not seen large deviations in the scatter plots, neither in the τ_{200}/A_V nor in the dust temperature derivation, as reflected in the uncertainties in T_d and τ_{200}/A_V . Extremely high, local emissivities are expected to show up in these scatter plots, and are therefore excludable in our fields at the resolution we adopted, namely 3.5 arcmin.

5.2 Changes of dust properties at low temperature

Below 14 K, all τ_{200}/A_V values are higher than $2.4 \times 10^{-4} \text{ mag}^{-1}$, the representative value of the DISM. This finding agrees with the results of several earlier papers (see Section 1 and the caption of Fig. 2). The majority of our data points are within a well-defined range, 1–2 times the emissivity of the DISM. Enhanced emissivity values are usually interpreted as the change of dust properties: coagulation of dust particles or formation of ice mantles on grain surfaces (see e.g. Dwek 1997). Dust grains may show a large variety both in composition (silicate, carbon or mixed) and in structure (ice mantle, particle–cluster aggregates, cluster–cluster aggregates) and the different types show different enhancement of the emissivity. Since the emissivity enhancement typically is not higher than a factor of 2, our results are consistent with ice mantles or cluster of silicate particles (CCA or PCA, see Fig. 6). On the other hand, FIR emissivities produced by grains containing carbon aggregates are too high for most of our observed emissivity values. However, in some particular regions the observed τ_{200}/A_V exceeds significantly the representative values of the DISM, and may indicate the existence of carbonaceous grains.

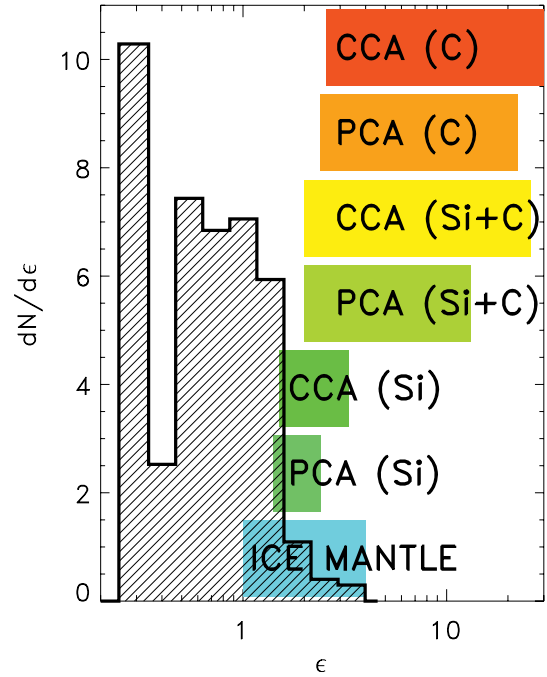


Figure 6. The histogram with shaded area shows the relative frequency ($dN/d\epsilon$) of the observed τ_{200}/A_V values relative to that of the DISM ($\epsilon = \tau_{200}/A_V / [\tau_{200}/A_V]_{\text{DISM}}$, where $[\tau_{200}/A_V]_{\text{DISM}} = 2.4 \times 10^{-4} \text{ mag}^{-1}$), found for our targets. Horizontal bars represent the predicted range of enhancement in emissivity for different types of grains following Stognienko, Henning & Ossenkopf (1995) from bottom to top: (i) ice mantles, (ii) silicate particle–cluster aggregates, (iii) silicate cluster–cluster aggregates, (iv) mixed (silicate and carbon) particle–cluster aggregates, (v) mixed cluster–cluster aggregates, (vi) carbon particle–cluster aggregates and (vii) carbon cluster–cluster aggregates.

5.3 Emissivities lower than in the DISM

As presented in Section 3.3 and Fig. 2, we find low emissivity values for $14 \text{ K} \leq T_d \leq 16 \text{ K}$ colour temperatures. Similar results were obtained for some specific regions by Lehtinen et al. (2004) and Rawlings et al. (2005). Even though one can explain an emissivity lower than that of the DISM in terms of changed grain properties, it is also possible to explain this behaviour using a bimodal temperature model (Cambr sy et al. 2001; del Burgo et al. 2003). In this model, we assume that the observed FIR surface brightness is due to two emission components with different dust temperatures, both due to big grains. The observed IR emission can be written as

$$I_\nu = \tau_{\nu,c} B_\nu(T_c) + \tau_{\nu,w} B_\nu(T_w), \quad (3)$$

where T_c and T_w are the temperatures of the cold and warm dust components, respectively, and $\tau_{\nu,c}$ and $\tau_{\nu,w}$ are the IR optical depths of the cold and warm components, respectively. The emissivity of the cold component may differ from that of the warm component, and this change is characterized by the ϵ parameter:

$$\tau_{\nu,c} = \epsilon X \tau_{\nu,\text{tot}}, \quad (4)$$

$$\tau_{\nu,w} = (1 - X) \tau_{\nu,\text{tot}}, \quad (5)$$

where $\tau_{\nu,\text{tot}}$ is the total effective optical depth if both components had identical emission properties and X is the fraction of the optical depth of the cold component with respect to the effective total opacity (for more details, see del Burgo et al. 2003). In del Burgo et al. (2003),

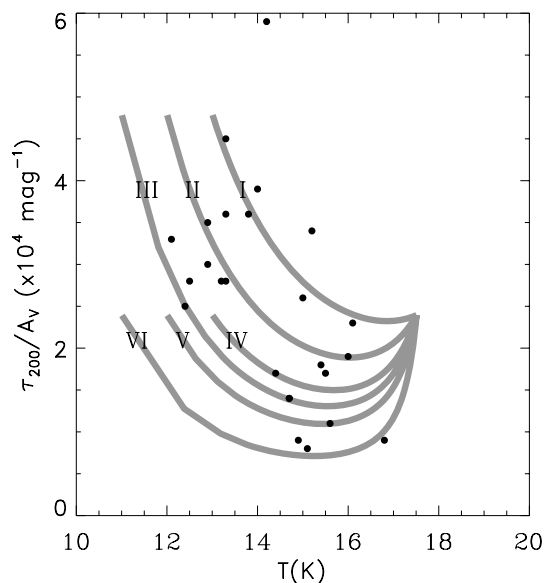


Figure 7. In this figure, we present model fits of T_d versus τ_{200}/A_V with a dust emission of bimodal temperature distribution. The grey curves represent different emissivities and cold temperatures (T_c). To derive the ‘virtual’ dust temperature, surface brightness at 100 μm (short) and 200- μm (long) wavelengths were used. The warm dust temperature has been set to $T_w = 17.5$ K. Other short wavelengths (90 or 120 μm) produce curves very close to the 100- μm ones. (I) $\epsilon = 2.0$, $T_c = 13.0$ K; (II) $\epsilon = 2.0$, $T_c = 12.0$ K; (III) $\epsilon = 2.0$, $T_c = 11.0$ K; (IV) $\epsilon = 1.0$, $T_c = 13.0$ K; (V) $\epsilon = 1.0$, $T_c = 12.0$ K; (VI) $\epsilon = 1.0$, $T_c = 11.0$ K. The black dots mark our measured τ_{200}/A_V values.

the cold temperature T_c was chosen to be 13.5 K, representing the lowest colour temperatures obtained from their sample. However, in our sample we included denser molecular regions and the presence of colour temperatures of $T_d \approx 12$ K obviously requires a lower T_c value.

We derived the colour temperature from the slope of the scatter plot of two IR-wavelength surface brightness distributions. It is easy to see that in a bimodal temperature distribution the variation of X causes a change in the ratio of surface brightness values measured at two wavelengths (see fig. 8 in del Burgo et al. 2003), i.e. an effect very similar to the change of the colour temperature. A specific X value can be directly linked to a ‘virtual’ colour temperature, as long as T_c and T_w are fixed. As we demonstrate below, mixing rather than change of dust grain properties can be the reason that data points in Fig. 2(b) fall below the representative value of the DISM. In Fig. 7, we plot τ_{200}/A_V model curves with mixing ratios changing in the $0 \leq X \leq 1$ range versus the corresponding virtual colour temperature. In this model, we used $\tau_{v,\text{tot}} = 2.4 \times 10^{-4} \text{ mag}^{-1}$, which is the representative value of the DISM (Schlegel, Finkbeiner & Davis 1998). In all cases, we kept $T_w = 17.5$ K and assumed different values of T_c . For ϵ , either $\epsilon = 1$ or $\epsilon = 2$ was adopted.

It is clear from Fig. 7 that in order to reproduce the higher τ_{200}/A_V values for cold regions ($T < 14$ K), the emissivity of the cold component in the bimodal model has to be enhanced.

It is noteworthy, however, that the observed low τ_{200}/A_V values ($14 \leq T \leq 16$ K) can be well fitted by using $\epsilon = 1$ for both the warm and cold components.

This result suggests that the presence of colder component with the same grain properties as for the DISM is sufficient to explain the low τ_{200}/A_V in a region. The most plausible reason is that radiative transfer in these regions can cause some parts to become colder while

our temperature measurement is biased towards the warmer regions. However, a necessary condition is that the colder component is well mixed and not resolved by ISOPHOT; otherwise the scatter diagrams would become highly non-linear. Whether this can be achieved in a cloud model needs to be investigated.

5.4 Smaller grains

An alternative explanation for low emissivity clouds with low column density is an enhancement of the relative contribution of small grains, since for a grain size a , $Q_{\text{abs}} \propto a$ in the FIR. If this is a likely mechanism, then the regions with τ_{200}/A_V lower than the DISM would have undergone some recent processing such that the relative amount of small grains is larger than in the standard grain size distribution. We note that a fraction of the clouds was selected from the *IRAS* data on the basis of the high 100- μm brightness. These clouds also exhibit a high brightness in the *IRAS* 12-, 25- and 60- μm bands and could indicate a bias towards clouds with a grain size distribution favouring the smaller sizes.

6 CONCLUSIONS

In this paper, we have analysed the FIR emission properties in a large sample of interstellar clouds observed with ISOPHOT. We have derived FIR emissivity relative to the visual extinction, τ_{200}/A_V , for each region. The derived values of τ_{200}/A_V represent the average emissivity over a region typically of the order of 100 arcmin².

The derived FIR emissivities τ_{200}/A_V show an enhancement for the coldest and densest regions where $12 \text{ K} \leq T_d \leq 14 \text{ K}$, which is most probably due to the growth of dust grains. We confirm a similar trend found in earlier papers.

The enhancement of τ_{200}/A_V for $12 \leq T_d \leq 14$ K is for the majority of the regions less than 2. This is lower than that previously reported for some specific clouds. Our findings support models where the enhancement in emissivity is attributed to ice mantle growth and the presence of silicate aggregates on the spatial scales we investigated.

For $14 \leq T_d \leq 17.5$ K, we observe a majority of regions where τ_{200}/A_V is lower than that of the DISM. FIR emissivities lower than that of the DISM may be explained by the common effect of a constant emissivity and the presence of multiple dust temperatures along the line of sight. To sufficiently fit the observed values, the cold temperatures (T_c) had to be set to ~ 12 K without significantly altering the dust properties. Alternatively, these clouds in our sample could be biased towards regions with a more significant small grain component in their dust size distribution.

ACKNOWLEDGMENTS

We thank the referee Dr Mika Juvela for detailed comments and suggestions which helped us to improve the manuscript. This paper is based on observations with *ISO* an ESA project with instruments funded by ESA member states (especially the PI countries: France, Germany, the Netherlands and the United Kingdom) and with participation of ISAS and NASA. The *ISOPHOT* data were processed using PIA, a joint development by the ESA Astrophysics Division and the *ISOPHOT* consortium led by MPI für Astronomie, Heidelberg. Contributing Institutes are DIAS, RAL, AIP, MPIK and MPIA.

This research has made use of the following catalogues/services:

- (i) USNOFS Image and Catalogue Archive, operated by the United States Naval Observatory, Flagstaff Station (<http://www.nofs.navy.mil/data/fchpix/>)

(ii) NASA/IPAC Infrared Science Archive, which is operated by the Jet Propulsion Laboratory, California Institute of Technology, under contract with the National Aeronautics and Space Administration (the 2MASS Point Source Catalogue)

(iii) ISO Data Archive, European Space Astronomy Centre of the European Space Agency (<http://www.iso.esac.esa.int/ida/>)

This research has been supported by the grants T34584 and K62304 of the Hungarian Research Fund (OTKA).

REFERENCES

- Arendt R. G. et al., 1998, *ApJ*, 508, 74
 Bernard J. et al., 1999, *A&A*, 347, 640
 Bianchi S., Gonclaves J., Albrecht M., Caselli P., Chini R., Galli D., Walmsley M., 2003, *A&A*, 399, L43
 Boulanger F., Abergel A., Bernard J.-P., Burton W. B., Desert F.-X., Hartmann D., Lagache G., Puget J.-L., 1996, *A&A*, 312, 256
 Cambrésy L., Epchtein N., Copet E., de Batz B., Kimeswenger S., Le Berte T., Rouan D., Tiphene D., 1997, *A&A*, 324, L5
 Cambrésy L., Boulanger F., Lagache G., Stepnik B., 2001, *A&A*, 375, 999
 Cambrésy L., Beichman C. A., Jarrett T. H., Cutri R. M., 2002, *AJ*, 123, 2559
 Cardelli J. A., Clayton G. C., Mathis J. S., 1989, *ApJ*, 345, 245
 Cutri R. M., Skrutskie M. F., van Dyk S., 2003, 2MASS All-Sky Catalog of Point Sources, VizieR On-line Data Catalog: II/246
 del Burgo C., Laureijs R. J., 2005, *MNRAS*, 360, 901
 del Burgo C., Laureijs R. J., Ábrahám P., Kiss Cs., 2003, *MNRAS*, 346, 403
 Draine B. T., Lee H. M., 1984, *ApJ*, 285, 89
 Dupac X. et al., 2003, *A&A*, 404, L11
 Dwek E., 1997, *ApJ*, 484, 779
 Gabriel C., Acosta-Pulido J., Heinrichsen I., Morris H., Tai W.-M., 1997, in Hunt G., Payne H. E., eds, ASP Conf. Ser., Vol. 125, *Astronomical Data Analysis Software and Systems VI*. Astron. Soc. Pac., San Francisco, p. 108
 Gezari D. Y., Joyce R. R., Simon M., 1973, *ApJ*, 179, L67
 Hauser M. G., Arendt R. G., Kelsall T., 1998a, *ApJ*, 508, 25
 Hauser M. G., Kelsall T., Weiland J., eds, the COBE Science Working Group, 1998b, *COBE Diffuse Infrared Background Experiment (DIRBE) Explanatory Supplement*, Version 2.3 (1998 January 14) (<http://lambda.gsfc.nasa.gov/product/cobe/dirbe'exsup.cfm>)
 Juvela M., Mattila K., Lehtinen K., Lemke D., Laureijs R. J., Prusti T., 2002, *A&A*, 382, 583
 Kiss Z., Tóth L. V., Krause O., Kun M., Stickel M., 2006, *A&A*, 453, 923
 Klaas U. et al., 2003, in Metcalfe L., Salama A., Peschke S. B., eds, *The Calibration Legacy of the ISO mission*, ESA SP-481. ESA Publications, Noordwijk, p. 19
 Lada C. J., Lada E. A., Clemens D. P., Bally J., 1994, *ApJ*, 429, 694
 Lagache G., Abergel A., Boulanger F., Puget J.-L., 1998, *A&A*, 333, 709
 Laureijs R. J., Klaas U., Richards P. J., Schulz B., Ábrahám P., 2003, *The ISO Handbook*, Vol. V, PHT – The Imaging Photo-Polarimeter, Version 2.0.1, ESA SP-1262. ESA Publications Division, Noordwijk
 Lehtinen K., Lemke D., Mattila K., Haikala L. K., 1998, *A&A*, 333, 702
 Lehtinen K., Russeil D., Juvela M., Mattila K., Lemke D., 2004, *A&A*, 423, 975
 Lemke D. et al., 1996, *A&A*, 315, L64
 Lombardi M., Alves J., 2001, *A&A*, 337, 1023
 Monet D. G., Bird A., Canzian B., 1998, *The USNO-A2.0 Catalogue*, VizieR On-line Data Catalog: I/252 (originally published in US Naval Observatory Flagstaff Station (USNOFS) and, Universities Space Research Association (USRA) stationed at USNOFS)
 Monet D. G., Levine S. E., Canzian B., 2003, *AJ*, 125, 984
 Moór A., Ábrahám P., Kiss C., Csizmadia S., 2003, *Far-Infrared Observations of Normal Stars Measured with ISOPHOT in Mini-Map Mode*. Report on Highly Processed Data Products, Version 1.1 (http://pma.iso.vilspa.esa.es:8080/hdpdp/technical_reports/technote38.html)

- Moór A., Ábrahám P., Kiss C., Csizmadia S., 2004a, *Far-Infrared Observations of Evolved Stars Measured with ISOPHOT in Mini-Map Mode*. Report on Highly Processed Data Products, Version 1.0 (http://pma.iso.vilspa.esa.es:8080/hdpdp/technical_reports/technote40.html)
 Moór A., Ábrahám P., Kiss C., Csizmadia S., 2004b, *Far-Infrared Observations of Normal Miscellaneous Objects Measured with ISOPHOT in Mini-Map Mode*. Report on Highly Processed Data Products, Version 1.0 (http://pma.iso.vilspa.esa.es:8080/hdpdp/technical_reports/technote41.html)
 Moór A., Ábrahám P., Kiss C., Csizmadia S., 2005, *Far-Infrared Observations of Extragalactic Objects Measured with ISOPHOT in Mini-Map Mode*. Report on Highly Processed Data Products, Version 1.0 (http://pma.iso.vilspa.esa.es:8080/hdpdp/technical_reports/technote30.html)
 Pagani L. et al., 2003, *A&A*, 406, L59
 Rawlings M. G., Juvela M., Mattila K., Lehtinen K., Lemke D., 2005, *MNRAS*, 356, 810
 Ridderstad M., Juvela M., Lehtinen K., Lemke D., Liljeström T., 2006, *A&A*, 451, 961
 Salama A., 2004, 35th COSPAR Scientific Assembly, Recent Highlights from the *Infrared Space Observatory*. p. 4681
 Salama A., Ortiz I., Arviset C., 2004, in Ochsenbein F., Allen M. G., Egret D., eds, ASP Conf. Ser., Vol. 314, *User Provided Reduced Data, Catalogues and Atlases in the ISO Data Archive*. Astron. Soc. Pac., San Francisco, p. 26
 Schlegel D. J., Finkbeiner D. P., Davis M., 1998, *ApJ*, 500, 525
 Stepnik B. et al., 2003, *A&A*, 398, 551
 Stognienko R., Henning Th., Ossenkopf V., 1995, *A&A*, 296, 797
 Whittet D. C. B., Gerakines P. A., Hough J. H., Shenoy S. S., 2001, *ApJ*, 547, 872
 Wolf M., 1923, *Astron. Nachr.*, 219, 109

APPENDIX A: COMPARISON OF THE ISOPHOT AND COBE/DIRBE SURFACE BRIGHTNESS PHOTOMETRIC SYSTEMS

The calibrational accuracy of the ISOPHOT surface brightness photometric system is crucial for the interpretation of the final results. Due to the lack of proper extended standard objects on the sky, especially at FIR wavelengths, the only practical possibility to test the accuracy is a comparison of ISOPHOT data with that of COBE/DIRBE values. Here first we check the general relationship between the ISOPHOT and COBE/DIRBE surface brightness systems via the comparison of P22 minimap highly processed data product (HPDP) background values from the ISO Data Archive. In a second approach, average surface brightness values of our target fields of the present study, obtained from ISOPHOT observations is compared with those derived from COBE/DIRBE surface brightness data.

A1 Description of the COBE/DIRBE background determination

The monochromatic COBE/DIRBE surface brightness value at a specific wavelength, date and sky position is derived with the PREDICTDIRBE tool, written in IDL² and developed in Konkoly Observatory, using some routines written at Max-Planck-Institut für Astronomie, Heidelberg. The PREDICTDIRBE routine uses the CGIS³ software library, developed to help the analysis of COBE data. PREDICTDIRBE uses two main DIRBE data products, the DIRBE sky and

² Research Systems Inc., Versions 5.x and 6.x

³ <http://lambda.gsfc.nasa.gov/product/cobe/cgis.cfm>

zodi atlases (DSZA) and the zodi-subtracted mission average maps (ZSMA). The detailed description of these DIRBE data products can be found on the *COBE*/DIRBE homepage of IPAC.⁴ The main steps of the *COBE*/DIRBE surface brightness determination in the PREDICTDIRBE routine are the following.

(i) *Extraction of DIRBE ZSMA (zodiacal light component removed) surface brightness values for the 10 DIRBE photometric bands.* The number of DIRBE pixels considered here as well as for the determination of the zodiacal contribution depends on the extension of ISOPHOT maps. However, the spatial sampling of DIRBE measurements at long wavelengths is very fine relative to the physical resolution (~ 30 arcmin or worse). The operations below are done for the median values of the DIRBE pixels taken.

(ii) *Colour correction of the cirrus component.* In this step the temperature of the cirrus component is determined by fitting the 100-, 140- and 240- μm ZSMA surface brightness values with a modified blackbody spectral energy distribution (SED), $I_\nu \propto \nu^\beta B_\nu(T)$, where $B_\nu(T)$ is the Planck function at temperature T and frequency ν , and β is the spectral index. The 140- μm DIRBE band has a lower weight in the fitting process, due to its well-known noisy behaviour compared to the other bands. For our calculations the spectral index has been fixed to $\beta = 2$. For $\lambda < 100 \mu\text{m}$ the SED is approximated by a function fitted by spline interpolation to the measured $\log(\lambda) - \log(I_\lambda^{\text{DIRBE}})$ values. The colour correction is performed using the fitted SEDs, and the transmission curves of the DIRBE filters. The final, monochromatic surface brightness values are reached by the repetition of this process, until the convergence criterion is matched. We have to note that the ZSMA surface brightness contains at least two main components: the cirrus (or, in general Galactic interstellar matter) emission and the extragalactic background. Although the two components have different SEDs, the difference between colour corrections needed for the two different SEDs is small, and in most cases the absolute level of the extragalactic background component is much below that of the cirrus. Therefore here we do not consider these two components separately.

(iii) *Determination of the non-zodiacal DIRBE surface brightness at the ISOPHOT wavelength.* The monochromatic DIRBE surface brightness values are interpolated to the nominal ISOPHOT filter wavelength. For $\lambda < 100 \mu\text{m}$ this is performed by the spline interpolation of the $\log(\lambda) - \log(I_\lambda^{\text{DIRBE}})$ values, while for $\lambda \geq 100 \mu\text{m}$ the previously mentioned $\nu^\beta B_\nu(T)$ is applied.

(iv) *The zodiacal component* is determined from the DIRBE zodi atlases (DSZA products). From the date of the observation the actual solar elongation angle of the requested sky coordinate is calculated. In case no DIRBE observation was performed at that solar elongation and ecliptic latitude (due to the limited lifetime of the instrument), the actual solar elongation is ‘mirrored’, so that the solar elongation with the same absolute value is taken on the other side of the Sun, and the zodiacal component is extracted at the corresponding dates and coordinates. This latter position was in almost all cases observed by DIRBE (for the details of *COBE*/DIRBE observations, see Hauser et al. 1998b). The zodiacal component is extracted for all the 10 DIRBE photometric bands.

(v) *Colour correction of the zodiacal component* is performed assuming a pure blackbody SED around the peak of the zodiacal emission, and using spline interpolation for notably shorter and longer wavelengths, applying otherwise the same iterative process as for

the colour correction of the non-zodi component above. The resulting monochromatic zodiacal surface brightness values are used to interpolate to the requested ISOPHOT wavelength.

(vi) *The final PREDICTDIRBE surface brightness* is the sum of the monochromatic zodiacal and the non-zodiacal (cirrus + extragalactic background) components.

A2 Minimaps HPDPs

Minimap mode was a ‘submode’ of the P22 astronomical observing template (AOT, see Laureijs et al. 2003) of ISOPHOT. The mode was especially designed to obtain accurate fluxes of point/compact sources. However, apart from the point source flux determination, the minimaps provide accurate surface brightness values of the average background around the target, due to the redundant observation of the same sky position by many ISOPHOT pixels. The minimap backgrounds are assumed to be homogeneous for the whole minimap area. The typical spatial extension of a minimap is ~ 4 arcmin for both the C100 and the C200 detector arrays.

The background values can be compared with the values obtained by the PREDICTDIRBE routine for the specific central coordinates of the source (assuming a 30-arcmin aperture) and for the ISOPHOT wavelengths. Moór et al. (2003, 2004a,b, 2005) performed a full re-evaluation of a large sample of ISOPHOT minimaps, containing the observations of normal stars, evolved stars, extragalactic and miscellaneous objects. The publicly available *ISO* Data Archive⁵ contains the re-evaluated results of these observation as HPDPs (Salama, Ortiz & Arviset 2004).

The results of the *COBE*/DIRBE and minimap background comparisons are presented in Fig. A1 for the four ISOPHOT filters used in our study (90, 100, 120 and 200 μm). In Table A1 we present the coefficients found for the correlation between the DIRBE and ISOPHOT surface brightness photometric systems, assuming the linear relationship

$$I_\lambda^{\text{ISOPHOT}} = S \times I_\lambda^{\text{DIRBE}} + \text{Offset}, \quad (\text{A1})$$

where $I_\lambda^{\text{ISOPHOT}}$ and I_λ^{DIRBE} are the surface brightness values at the wavelength λ , measured with ISOPHOT and DIRBE, respectively.

The last two columns of Table A1 contain the mean relative deviations of original ISOPHOT and DIRBE surface brightness values (Column 4) and the mean relative deviations of the original ISOPHOT and DIRBE surface brightness values after the correction with the fitted line (‘residual scatter’, Column 5). These values are representative for the general relative accuracy of the two photometric systems.

The DIRBE surface brightness calibration (as well as that of ISOPHOT) contains intrinsic uncertainties, both in detector gain and offset. These uncertainties contribute significantly to the observed relative deviations listed in Table A1. For those DIRBE filters that are important for the comparison with the ISOPHOT surface brightness calibration in this paper, the typical gain uncertainties are 13.5 per cent, 10.6 per cent and 11.6 per cent for the 100-, 140- and 240- μm DIRBE bands, respectively (see Arendt et al. 1998). These DIRBE gain uncertainties indicate the presence of an additional uncertainty of the order of ~ 10 per cent or below, which should account for the uncertainties in the PREDICTDIRBE estimate calculation as well as in the intrinsic uncertainties of the ISOPHOT calibration.

The typical offset uncertainties are 0.3, 0.6 and 0.4 MJy sr^{-1} for the 100-, 140- and 240- μm DIRBE bands per pixel, respectively

⁴ http://lambda.gsfc.nasa.gov/product/cobe/dirbe_overview.cfm

⁵ <http://www.iso.vilspa.esa.es/ida/index.html>

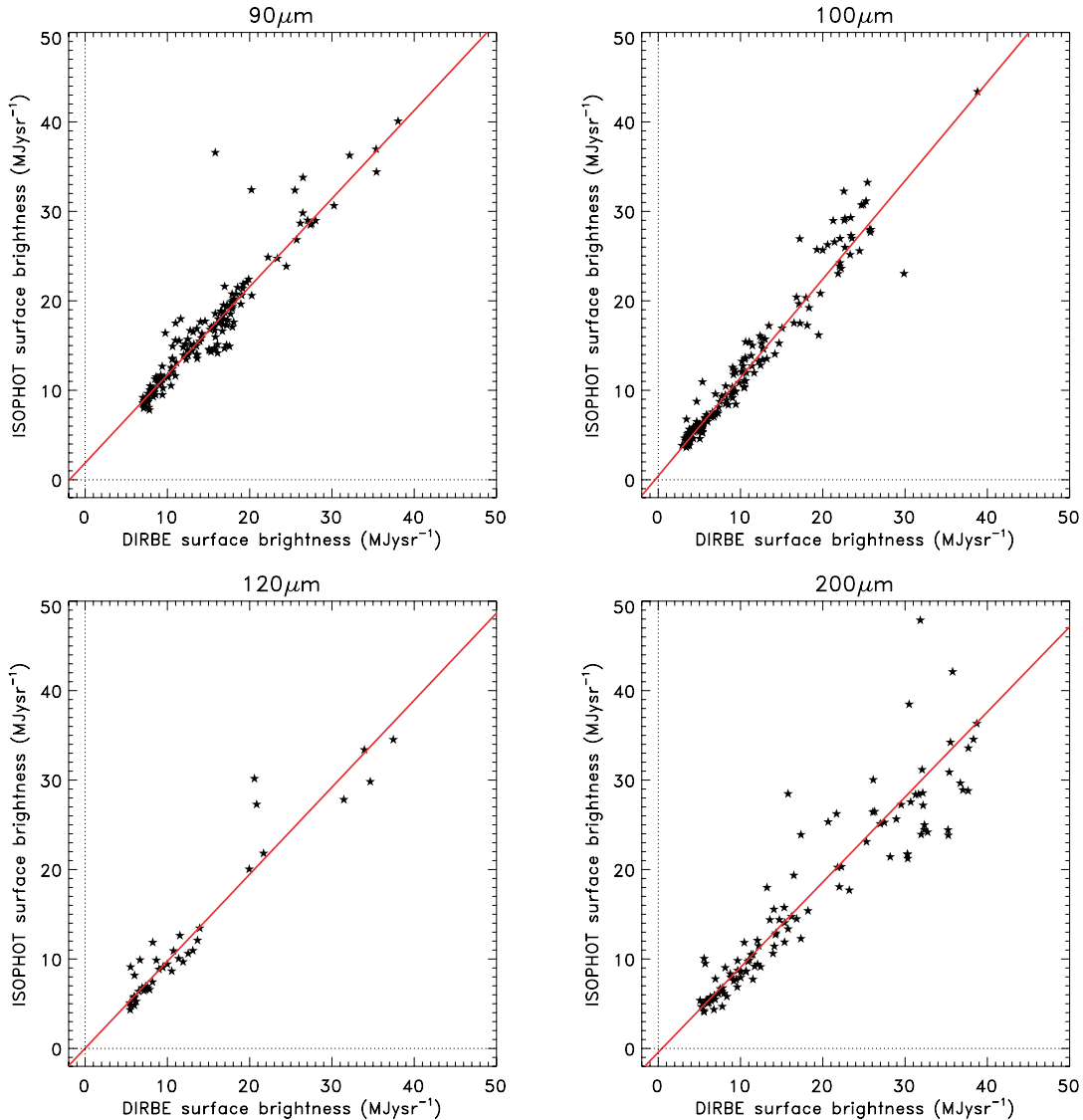


Figure A1. Comparison of minimap background surface brightness values and background estimates based on *COBE*/DIRBE data at different wavelengths (a) 90 μm , (b) 100 μm , (c) 120 μm and (d) 200 μm . The solid lines are fitted lines, corresponding to the values in Table A1.

(Arendt et al. 1998). These are of the order of the offset values found for the ISOPHOT–DIRBE comparison (see Table A1), except for the 90- μm ISOPHOT filter, where this offset is significantly higher. However, the 90- μm surface brightness values may also contain an emission contribution from a grain population different from the one responsible for the $\lambda \geq 100 \mu\text{m}$ part of the background SED. This effect is not accounted for in the PREDICTDIRBE routine.

In the case of ISOPHOT, non-unity scaling factors may arise from imperfect knowledge of the effective solid angles at different wavelengths and/or from a flux-dependent non-linearity of the detector. ISOPHOT solid angles have been reassessed recently (Ábrahám et al., private communication) and the new values agree within 5 per cent with the previous ones. Non-linearity can occur due to calibration uncertainties in the extrapolation to weak flux levels because the ISOPHOT calibration targets were always much brighter than the ISM in the ISOPHOT beams. The importance of the non-linearity can be estimated via comparison with the *COBE*/DIRBE calibration. According to the results presented in

Table A1 the relationships between the ISOPHOT and *COBE*/DIRBE surface brightness values are sufficiently linear.

A3 Fields of the present study

The target fields of the present study were observed by the same AOT (P22) as the minimaps, with some notable differences between the two samples. First, the extension of the target field maps is in the 5–40 arcmin range, while the minimaps are smaller than these. Second, the intensity of the target maps contains the contribution of point sources and also that of larger scale structures, while the point source emission was subtracted in the derivation of the minimap backgrounds.

The average surface brightness of our target fields was derived as simple average of all pixel values, for both the short and the long wavelength maps of a specific field. PREDICTDIRBE estimates of the DIRBE surface brightness were calculated for the central positions of the ISOPHOT maps. The observational date of the maps were also considered to account for the annual variation of the

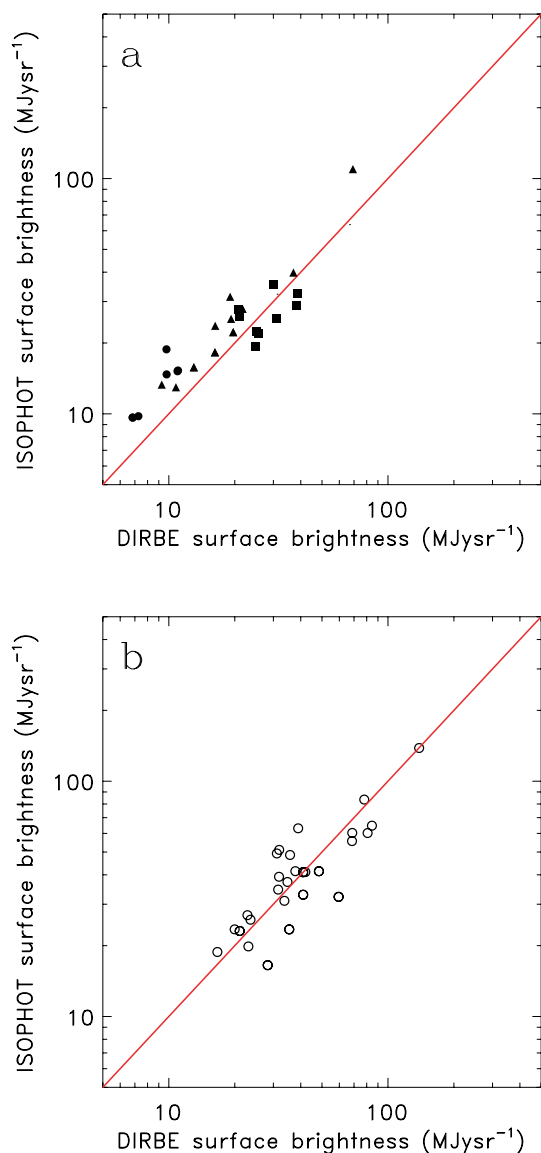


Figure A2. Comparison of the average surface brightness of our target fields and the DIRBE surface brightness derived for the same sky positions and observational dates, with the PREDICTDIRBE routine. (a) Short wavelength filters (ISOPHOT 90, 100 and 120 μm , marked by filled circles, triangles and squares, respectively); (b) ISOPHOT 200- μm filter. The solid lines mark the 1:1 line.

zodiacal light component. The results are presented in Fig. A1 and in Table A2.

A4 Summary

The results of the DIRBE and ISOPHOT surface brightness comparisons can be summarized as follows.

(i) In general a very good linear relationship was found between the ISOPHOT and DIRBE surface brightness photometric systems.

(ii) The scaling factors between the DIRBE and the ISOPHOT surface brightness photometric systems are close to unity, within the uncertainties. Even largest difference (100 μm) is within 9 per cent to the DIRBE system. These scaling factors indeed have an impact on the derived dust temperatures and τ_{200}/A_V ratios. This

Table A1. Parameters describing the relation between the DIRBE and ISOPHOT surface brightness photometric systems, derived from the minimap HPDP sample, assuming a linear relationship. The columns of the table are: (1) ISOPHOT filter nominal wavelength; (2) fitted scaling factor (S), assuming equation (A1); (3) fitted offset, assuming equation (A1); (4) mean relative deviation of original ISOPHOT and DIRBE surface brightness values; (5) mean relative deviation of ISOPHOT and DIRBE surface brightness values after the correction with the fitted line.

λ (μm)	S	Offset (MJy sr^{-1})	$R_{1:1}$ (per cent)	R_f (per cent)
90	$0.98(\pm 0.02)$	$1.87(\pm 0.13)$	14.2	8.5
100	$1.09(\pm 0.03)$	$0.43(\pm 0.13)$	16.7	10.5
120	$0.97(\pm 0.06)$	$0.02(\pm 0.28)$	12.8	11.4
200	$0.95(\pm 0.03)$	$-0.44(\pm 0.24)$	14.9	10.8

Table A2. The columns of the table are: (1) the name of the field (central galactic coordinates); (2) central wavelengths of the short/long ISOPHOT filters [$\mu\text{m}/\mu\text{m}$]; (3) short wavelength DIRBE surface brightness (MJy sr^{-1}); (4) short wavelength ISOPHOT surface brightness (MJy sr^{-1}); (5) long wavelength DIRBE surface brightness (MJy sr^{-1}); (6) long wavelength ISOPHOT surface brightness (MJy sr^{-1}).

Field	λ_s/λ_l	I_s^D	I_s^{PHT}	I_l^D	I_l^{PHT}
G004.3+35.8	100/200	19.0	31.5	38.9	63.1
G100.0+14.8	90/200	11.0	15.3	31.5	34.6
G101.8+17.0	100/200	10.8	13.0	23.1	19.9
G102.0+15.2	90/200	9.8	14.7	37.8	41.5
G114.0+14.9	120/200	24.8	19.3	41.0	32.9
G114.3+14.7	120/200	25.6	22.0	42.0	41.1
G114.6+14.6	120/200	25.2	22.5	41.0	41.0
G121.6+24.6	90/200	7.3	9.8	22.8	27.0
G122.0+24.2	90/200	6.8	9.6	21.1	23.1
G142.0+38.5	100/200	9.3	13.3	16.7	18.8
G170.2-16.0	120/200	31.1	25.3	48.4	41.4
G173.9-15.7	120/200	38.1	28.9	68.5	55.7
G174.3-15.9	120/200	38.6	32.6	68.7	60.3
G297.3-16.2	100/200	21.7	27.9	84.5	64.7
G300.2-16.8	120/200	9.8	18.8	31.8	39.2
G301.7-16.6	90/200	16.3	23.7	34.8	37.3
G302.6-15.9	100/200	13.0	15.8	28.3	16.5
G303.5-14.2	100/200	19.7	22.2	59.5	32.2
G303.8-14.2	100/200	16.2	18.3	35.4	23.5
G355.3+14.7	100/200	69.2	109.7	138.8	138.4
G359.1+36.7	100/200	19.2	25.3	23.6	25.8
G359.9-17.9	100/200	37.0	39.8	78.0	83.5
G089.0-41.2*	90/200	11.0	15.2	20.0	23.5
G111.2+19.6*	150/200	31.2	32.2	33.7	31.0
G187.3-16.7*	120/200	30.2	35.4	35.8	48.6
G297.3-15.7*	150/200	66.8	63.7	80.8	60.2
G301.2-16.5*	120/200	20.8	27.9	31.1	49.3
G301.7-16.6*	120/200	21.1	25.8	31.9	51.1

effect is widely discussed for the typical deviations in the main text (see Section 4.5).

(iii) The offsets found between the DIRBE and ISOPHOT surface brightness calibration based on the minimap data base are usually small (see Table A2). The largest offset value ($\sim 1.9 \text{ MJy sr}^{-1}$) is found for the ISOPHOT 90- μm filter. However, in this paper we applied the method of slope fitting in the derivation of dust temperature from surface brightness scatter plots and in the determination of the τ_{200}/A_V ratio, which is completely insensitive for offsets.

(iv) Not taking into account the systematic differences, the mean relative deviations between the ISOPHOT the *COBE*/DIRBE surface brightness values are within ~ 15 per cent for the four investigated wavelengths.

(v) The comparison of the ISOPHOT versus DIRBE relative deviations with the DIRBE intrinsic detector gain uncertainties and the ISOPHOT versus DIRBE offsets with the DIRBE intrinsic offset uncertainties show, that the uncertainties in the DIRBE surface brightness calibration have a significant impact on the ISOPHOT–DIRBE comparison. The DIRBE detector calibration uncertainties are at a similar level than other error sources (e.g. ISOPHOT detector calibration uncertainties, DIRBE background estimate uncertainties by the `PREDICTDIRBE` routine) and they may be dominant in some cases.

(vi) A representative ISOPHOT calibration uncertainty can be estimated by subtracting the DIRBE detector gain uncertainties (in

average ~ 12 per cent for the 100-, 140- and 240- μm DIRBE bands) from the mean relative deviations between the two photometric systems (in average ~ 15 per cent, see Column 4 in Table A1). The resulting value which we adopt for both short and long ISOPHOT wavelengths is 9 per cent.

(vii) The DIRBE and ISOPHOT surface brightness values in the target fields show a behaviour very similar to that of the minimap backgrounds. The general agreement between the ISOPHOT and DIRBE surface brightness values are very good. The relatively large deviations in some cases may be explained by the beamsize of DIRBE, which is large, even compared to the size of the ISOPHOT target maps.

This paper has been typeset from a $\text{\TeX}/\text{\LaTeX}$ file prepared by the author.